Experimental and modeling analysis of thermal runaway propagation over the large format energy storage battery module with $Li_4Ti_5O_{12}$ anode

Peifeng Huang [a], Ping Ping [b, c], Ke Li [a], Haodong Chen [a], Qingsong Wang [a, *], Jennifer Wen [c], Jinhua Sun [a]

[a] State Key Laboratory of Fire Science, University of Science and Technology of China, Hefei 230026, PR China

[b] College of Chemical Engineering, University of Petroleum of China, Qingdao 266580, PR China

[c] Warwick FIRE, School of Engineering, University of Warwick, Library Road, Coventry CV4 7AL,UK

Corresponding author: Q. Wang: State Key Laboratory of Fire Science, University of Science and Technology of China, Hefei 230026, PR China; email: pinew@ustc.edu.cn

Abstract

Insight of the thermal characteristics and potential flame spread over lithium-ion battery (LIB) modules is important for designing battery thermal management system and fire protection measures. Such thermal characteristics and potential flame spread are also dependent on the different anode and cathode materials as well as the electrolyte. In the present study, thermal behavior and flame propagation over seven 50Ah $Li(Ni_{1/3}Mn_{1/3}Co_{1/3})O_2/Li_4Ti_5O_{12}$ large format LIBs arranged in rhombus and parallel layouts were investigated by directly heating one of the battery units. Such batteries have already been used commercially for energy storage while relatively little is known about its safety features in connection with potential runaway caused fire and explosion hazards. It was found in the present heating tests that fire-impingement resulted in elevated temperatures in the immediate vicinity of the LIBs that were in the range of between 200 $^{\circ}$C and 900 $^{\circ}$C. Such temperature aggravated thermal runaway (TR) propagation, resulting in rapid temperature rise within the battery module and even explosions after 20 mins of "smoldering period". The thermal runaway and subsequent fire and explosion observed in the heating test was attributed to the violent reduction of the cathode material which coexisted with the electrolyte when the temperature exceeded 260 $^{\circ}$C. Separate laboratory tests, which measured the heat and gases generation from samples of the anode and cathode materials using C80 calorimeter, provided insight of the physical-chemistry processes inside the battery when the temperature reaches between 30 $^{\circ}$C to 300 $^{\circ}$C. The self-accelerating decomposition temperature of the cell, regarded as the critical temperature to trigger TR propagation, was calculated as 126.1 and 139.2 $^{\circ}$C using the classical Semenov and Frank-Kamenetskii models and the measurements of the calorimeter with the samples. These are consistent with the measured values in the heating tests in which TR propagated. The events leading to the explosions in the test for the rhombus layout was further analyzed and two possible explanations were postulated and

analyzed based on either internal catalytic reactions or Boiling Liquid Expansion Vapor Explosion (BLEVE).

Key words: Lithium ion battery safety; Thermal runaway propagation; Self-accelerating reaction temperature; Semenov and Frank-kamenetskii models; Catalytic reactions and BLEVE.

Nomenclature			
A	Pre-exponential factor (s^{-1})	T_0	Ambient temperature (K)
a_0	Reactant characteristic dimension	T_1	Temperature of vessel before heating (K)
Bi	Biot number	T_2	Temperature of vessel after heating (K)
C_p	Specific heat (J g^{-1} K^{-1})	T_a	Ambient temperature (K)
dH/dt	Overall heat flow (W)	T_s	Surface temperature of cell (K)
d	Reactant diameter (m)	T_{NR}	Temperature of no return (°C)
d_s	Thickness of separator (m)	T_{ing}	The ignition temperature (°C)
d_n	Thickness of anode material (m)	$T_{0(n)}$	Shell temperature at step n (K)
d_p	Thickness of cathode material (m)	$T_{NR(n)}$	Temperature of no return at step n
d_c	Thickness of collector (m)	V	Volumn (m^3)
d_u	Total thickness of a minimum unit in cell (m)	V_1	Volume of vessel before heating (m^3)
E	Activation energy (J mol^{-1})	V_2	Volume of vessel after heating (m^3)
E_a	Apparent activation energy (J mol^{-1})	***Greek letters***	
ΔHn	Reaction heat (J g^{-1})	ρ	Average density (g m^{-3})
HRR	Heat release rate (mW)	λ	Heat transfer coefficient (W m^{-1} K^{-1})
l	Reactant height (m)	λ_{ave}	Average thermal conductivity of cell (W m^{-1} K^{-1})
M	Mass of reactant (g)	λ_s	Thermal conductivity of separator (W m^{-1} K^{-1})
M_0	Initial mass of reactant (g)	λ_n	Thermal conductivity of anode material (W m^{-1} K^{-1})
n	Reaction order	λ_p	Thermal conductivity of cathode material (W m^{-1} K^{-1})
Δn	Variation of the amount of gases after heating	λ_c	Thermal conductivity of collector (W m^{-1} K^{-1})
P	Pressure (Pa)	δ_{cr}	Frank-Kamenetskii critical parameter
P_1	Pressure of vessel before heating (Pa)	χ	Equivalent surface heat transfer coefficient (W m^{-2} K^{-1})
P_2	Pressure of vessel after heating (Pa)	ε	Emissivity (W m^{-2} K^{-1})
q_G	Heat generation rate (J)	σ	Stefan-Boltzmann constant (W m^{-2} K^{-1})
q_L	Heat dissipation rate (J)	θ	Nondimensionalized temperature
r_b	Radius of cell		
r_1	Radius of mandrel		
R	Universal gas constant (J K^{-1} mol^{-1})		
R^2	Variance		
S	Surface area (m^2)		
SADT	Self-accelerating decomposition temperature (°C)		
SOC	State of charge (%)		
t	Time (s)		
T	Temperature of system (K)		

1. Introduction

Lithium-ion battery (LIB), as a basic energy storage unit, has been widely used in various electronic equipment and energy storage systems up to the level of megawatts [1, 2]. Many efforts have been directed towards the studying of anode and cathode materials with the aim to improve performance as well as safety. The properties of $Li_4Ti_5O_{12}$ (LTO) as the anode material have, in particular, been the subject of many recent studies. Its zero-strain insertion of lithium, no lithium plating with quick charging and high thermal stability compared with the carbon based anode render it is a promising candidate as the anode material for LIBs. However, the potential required for inserting Lithium into LTO is 1.5 V *vs* Li/Li+. This is higher than that for carbon based anode and not satisfactory to produce a lower voltage of the full cell, which means energy density of LIB with LTO as anode is to some extent limited, rendering it unsuitable for certain applications like electric vehicles [1-4]. However, some LIBs with LTO anode, such as the ones tested in this study, has found commercial applications in other areas, such as stationary energy storage. $Li(Ni_xCo_yMn_{1-x-y})O_2$ (NCM) is a widely-employed cathode material for LIBs. Comparing with other cathode materials like $LiCoO_2$, $LiFePO_4$ and $LiMn_2O_4$, NCM has higher specific capacity or energy density. NCM/LTO chemistry system for LIB is recognized to be a promising battery system owing to its longer working life and reliable cycling performance [5]. Furthermore, NCM/LTO battery not only has attractive performance in the form of coin cells, but also has excellent balance of high-energy, low temperature, and long-life performance as large format batteries [6].

Despite the promising potential for a wide range of energy applications, LIBs also have some inherent safety issues which need to be addressed from design stage to reduce the propensity to thermal runaway induced fire and explosion accidents in storage, transportation and utilization [3, 4, 7, 8]. Abnormal operating conditions such as thermal and electric abuse can easily lead to critical

failure of the LIB cells [9-20]. These abuse conditions can initiate a chain of exothermic reactions to cause temperature increase, which in turn accelerates the reaction rate [21, 22]. When this process becomes out of control, it could result in catastrophic ejection of gases or even combustion[23].

Recently, some methods have been developed to analyze the safety of LIBs. Eliud et al. [24] proposed a state of safety function that includes the effect of many sub-functions such as voltage, temperature, or mechanical deformation. Beelen et al. [25] developed a more-accurate approach based the impedance temperature. Various safety measures have also been introduced including the relief valve, novel separator, flame retardant additives, current interrupt (CID) and positive thermal coefficient (PTC) devices to decline the possibility and severity of failure at cell level [26-30]. Despite the progress, the risk of cell failure is still relatively high and increases with the storage capacity of the battery system. In large scale energy storage systems, hundreds or thousands of batteries are connected either in series or in parallel. Failure of a single cell would result in heat transfer through conduction and radiation to the surrounding cells, and potentially induce the catastrophic propagation of thermal runaway in the battery module[31].

A number of studies have been conducted on the fire hazard and failure mechanisms of LIBs. The failure of LIB is always triggered by successional exothermic side-reactions as breakdown of the solid-electrolyte interphase for the carbon based anode, melting of separator, cathode/anode reactions with electrolyte, decomposition of the electrolyte[32, 33]. Roth and co-workers in Sandia[34] investigated the thermal abuse performance of small 18650 LIB. They found that the thermal runaway response of LIB can be described as occurring in three stages marked by the temperature regimes: room temperature to 120 ^{o}C, onset of thermal runaway and 125 ^{o}C to 180 ^{o}C, venting and accelerated heating (smoke), 180 ^{o}C and above and explosive decomposition (flame). Liu et al. [35] measured the energy produced by flaming combustion and found that it is almost three times the

value of the energy generated inside the 18650 battery. Finegan et al. [36] tracked the evolution of the internal structural damage and thermal behavior during initiation and propagation of thermal runaway of 18650 LIBs by employing high-speed synchrotron X-ray computed tomography and radiography in conjunction with thermal imaging. These are all relatively small size LIBs. Large format batteries are more vulnerable and violent to thermal runaway as they contain more energy. Such batteries in high state of charge (SOC) have been found to emit jet fires following TR and present large temperature gradients from inside to surface when they failed [23, 37].

In LIB based energy storage system, it is important to prevent TR propagation to neighboring cells. Several models and experiments have been developed to investigate TR propagation in battery packs [38, 39]. Spotnitz et al. [38] and Feng et al. [35] numerically showed TR propagation over battery packs under using the exothermic behavior of a single cell and an energy balance which accounts for radiative, conductive, and convective heat transfer modes of the pack. The mechanism of TR propagation between adjacent cells was attributed to the cell failure at elevated the temperatures when the contact surface temperature was above the onset temperature of TR. As commented by Lopez [31], due to heat transfer between the adjacent cells, factors such as the spacing between the cells and the tab configuration may both affect TR propagation. Additionally, the electrical connectivity was also found to have considerable influence [40].

Despite the above important findings, the potential hazards of fire and its initiation in large format batteries have been largely overlooked by previous investigations apart very few publications [38,46]. Because of a larger interface between the cathode and anode as well as relatively high energy density, potential failure due to TR and its propagation could be more easily triggered, and if so more violent as well. The heat release rate (HRR) of combustion in the large format LIB they tested was measured as 1.7MW m^{-2} for a fully charged $LiMn_2O_4$/graphite cell. This is between the

HRR of gasoline and fuel oil [41]. Liu et al. [35] found that the maximum amount of energy released during flaming combustion was almost three times the amount of total energy inside the battery. The heat released during combustion is more likely to trigger TR propagation than heat transfer between the battery cells. In the meantime in large scale LIB applications which often has some confinement around the battery module, fire resulting from the TR of a single cell is likely to engulf the battery module and cause cascading effect.

Feng et al.[42]and Roth [43] analyzed the critical condition of battery TR based on the onset temperature through accelerating rate calorimeter (ARC) or differential scanning calorimeter (DSC). However, the onset temperature only indicates the initiation of heat release, the TR of the battery is affected by many factors including cell configuration, electrode materials and heat dissipation. Hatchard et al. [44] proposed and verified a critical threshold for inducing TR through laboratory tests and numerical simulations. This was also independently verified by Lopez et al. [17]. Potentially, the critical threshold could be more accurate to explain the TR propagation between cells than the onset temperature. However, few other studies have addressed this issue to further its development and application. On the other hand, a thermal self-ignition theory exists and often used to analyze the thermal risk of chemicals. In this approach, the thermal features of the side-reactions between the materials are used to predict and evaluate the thermal behavior of the systems through various models and assumptions [45, 46]. While this kind of correlation between the thermal behavior of LIB cell and thermal features of materials was only studied through simulations[17, 44], the thermal characteristics of the LIBs measured by ARC and DSC can also be further processed to analyze the thermal risk according to this theory. This approach can potentially provide more accurate analysis as it can include the influence of the above mentioned factors including cell configuration, thermal characteristics of electrode materials and boundary conditions.

In the present study, full-scale heating tests of large format energy storage battery modules were conducted in an ISO 9705 Full-Scale Room Fire test apparatus. The thermal behavior over the battery module was analyzed through the measurements of temperature, mass loss, combustion heat release and video recordings. The heat flow and gas generation from thermo-chemical reactions inside the battery were studied using the C80 calorimeter. Separate tests have also been conducted with samples of the electrode materials and the data obtained were used to provide input to the classical Semenov [47] and Frank-Kamenetskii [48] models to analyze the critical temperature and delay time of the battery that induces a self-accelerating reaction until TR. This is the first time that such analysis has been conducted.

2. Experimental set up and the instrumentation

2.1 The batteries and materials tested

Seven commercial 50Ah $Li(Ni_{1/3}Co_{1/3}M_{1/3})O_2$/LTO LIBs with polyethylene (PE)/polypropylene (PP) double layer separators, which are 66 mm in diameter and 260 mm long, have been tested. The cells are new and bought from the manufacturer. These LIBs were cycled twice to full state of charge (SOC) by cell cycle meter. The cans of cells are made of aluminum of 1.64 mm thick; and sealed through laser welding. There are tabs and relief valves on both sides of the LIBs. The designed actuate pressure for the safety valve is 0.5 MPa.

To obtain the thermal performance of charged materials, the materials same as test batteries need to be operated following the same procedure as described in our previous paper [49]. The cathode $Li(Ni_{1/3}Co_{1/3}Mn_{1/3})O_2$ and anode $Li_4Ti_5O_{12}$ disks were placed in the drying oven to be kept dry prior to the test. The electrolyte (ELE) is composed mainly of organic solvent (ethylene carbonate (EC), diethyl carbonate (DEC), dimethyl carbonate (DMC)) and $LiPF_6$. The mixture of the electrodes,

electrolyte and separators were assembled in a CR2032 coin cell in the glove box and cycled to full SOC for three times by the cell cycle meter. The materials were then extracted from the fully charged cells and transferred into a high-pressure stainless steel vessel for thermal and gas generation analysis.

2.2 The rig and its instrumentation

The experimental facility is the same as used in our previous publications [26]. As shown in Fig. 1, it mainly consists of an ISO9705 full-scale room fire test system, in which the heat release rate was measured through oxygen consumption. The rig is instrumented with digital video camera and Mettler electronic balance (METTLER TOLEDO XA32001L, 32.1kg capacity and $\pm$0.1g accuracy). Temperatures were measured by 1 mm K-type chromel–alumel thermocouples with a response time of 1 s and $\pm$1.5 ℃ accuracy. The schematic of the experimental set up is shown in Fig. 2. Four LIBs were arranged in rhombus and three in parallel layout to simulate the arrangement in practical situations. The cells were sieged by a steel mesh wire, which has a solid lower section of about 2 cm high from the base.

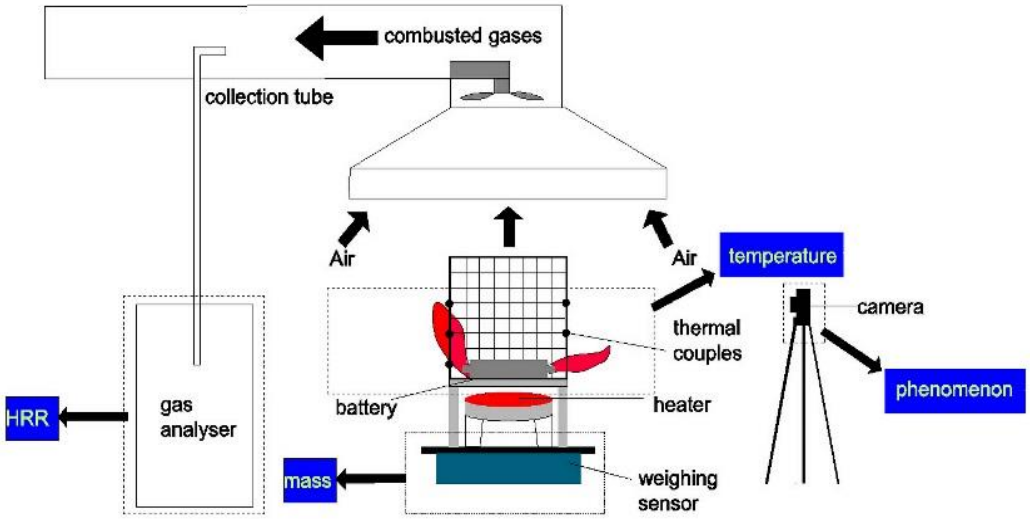

Fig. 1 Schematic of the experimental set up.

A radiant heater was placed underneath to provide thermal aggression at a constant rate of 5 kW

to the Number 2 (2#) LIB to mimic a fire environment. To exclude the influence of electric and heat transfer in the connecting rods, the electric power and connecting rods were not included in the tests. Some 33 mm thick fireproofing boards and gypsum boards were placed below the 1# and 4# LIBs to shade them from direct heating from the electric heater. A 12mm thick fireproofing board and a 9 mm thick gypsum board were placed separately under the 5# and 7# LIBs to provide partial shielding from the heat flux from below and extend the ignition time as shown in Fig. 2. The thermocouples were distributed in three regions, i.e. the surface, next to the tabs of the LIBs and around the LIBs for transient temperature measurements as shown in Fig. 2a for the rhombus layout. More specifically, thermocouple numbered as 1, 4, 5, 7 and 8 were placed to measure the temperatures at several locations on the surface of the LIBs; thermocouple numbered as 2, 3, 6, 9, 10 were used to measure the temperature of the tabs; additionally four thermocouple trees marked as A, B, C and D, were set at 85, 85, 85 and 225 mm away from the LIBs. The arrangement of the thermocouples for the tests for the three LIBs laid in parallel as shown in Fig. 2b was similar to that in Fig. 2a.

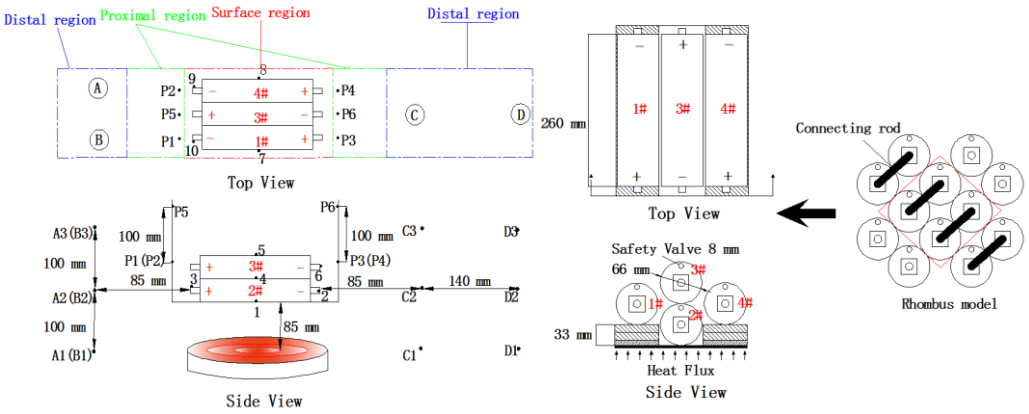

(a)

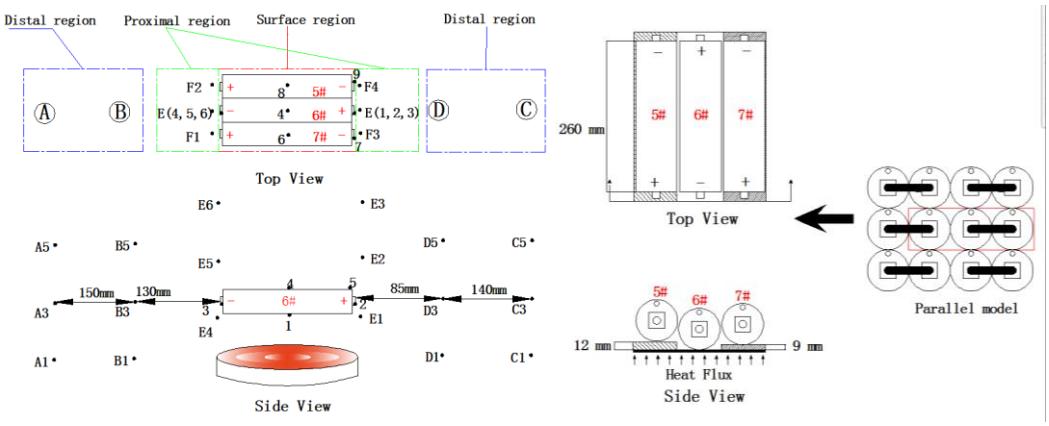

(b)

Fig. 2 Schematic of the battery and thermocouple arrangements: (a) four LIBs arranged in rhombus layout; (b) three LIBs arranged in parallel layout. The symbols A, B, C and D represent a series of thermocouples from side view.

To capture the sequence of events leading to thermal runaway of the NCM/LTO system and track the self-accelerating decomposition temperature, the CALVET micro calorimeter C80 was used to measure the heat flow released in the reaction of the electrode materials (NCM and LTO) in the presence of electrolyte at elevated temperature. The ranges for mass, pressure, temperature in the C80 experiments are 10 g, 350 bar and 300 ℃, respectively. Tand the uncertainty for pressure, temperature and heat flow measurements are $\pm$0.86 bar, $\pm$0.05 ℃ and $\pm$ 0.1 μw, which represent an improvement of almost 100 times in terms of sensitivity in comparison with the normal DSC. During the gas generation test, a pressure-sensitive transducer (Dynisco model PT435AH-5M-10/18) was used to monitor the variation of the pressure in the vessel. In line with the commercial battery, the mass ratio of electrode and electrolyte was set at 2:1. All the above operations except the cell cycling were carried out in the glove box to isolate the materials from air and water. The heating rate in the C80 test was set to limit the temperature increase to 0.2 °C per minute, and the temperature variation scale was set from 30 °C to 300 °C.

3. Results and discussion

3.1 The heating tests

3.1.1 Combustion behavior

The combustion characteristics of the flame spread over the LIBs arranged in both rhombus and parallel layouts are shown in Figs. 3 and 4, respectively.

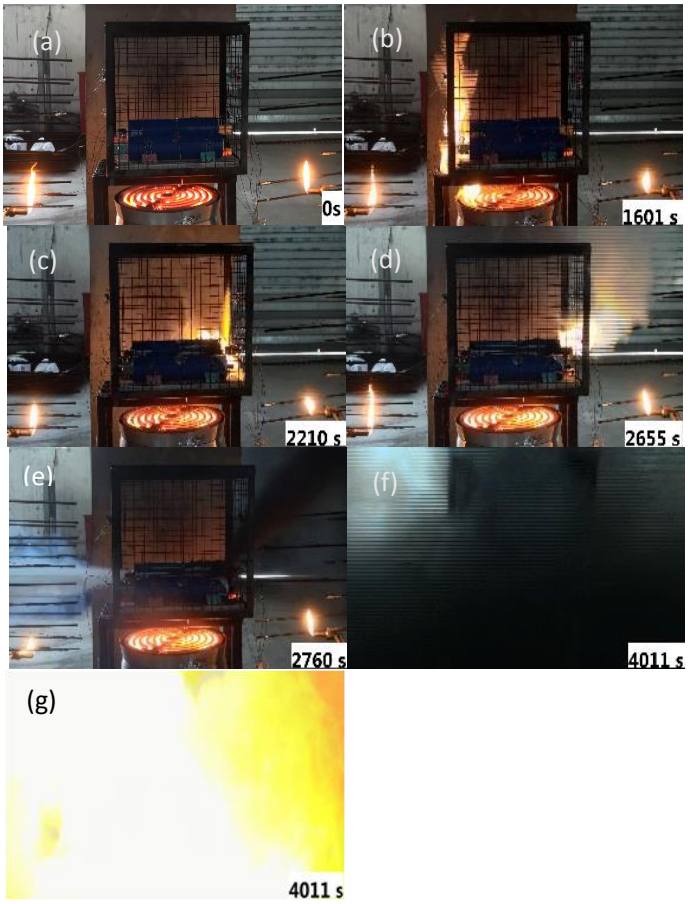

Fig. 3 The sequence of events during the heating test of the LIBs in rhombus layout. The interval time between figure (f) and (g) is less than 0.02 s.

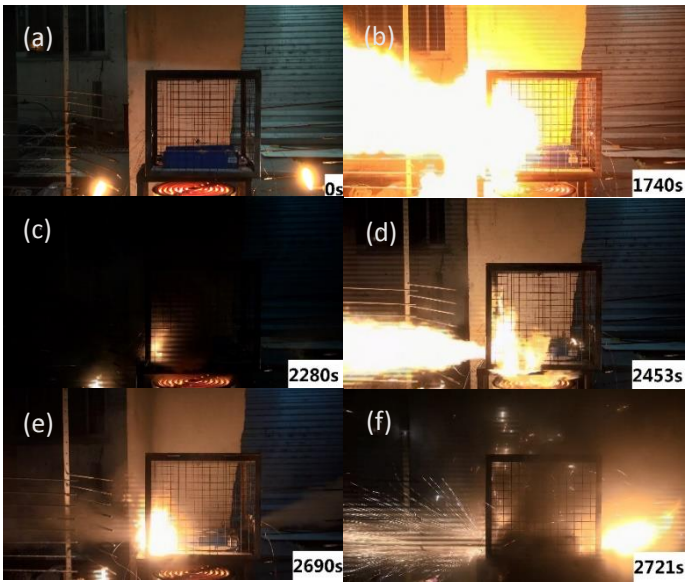

Fig. 4 The sequence of events during the heating test of the LIBs in parallel layout.

The sequence of events in the heating tests of the four LIBs in rhombus layout is recorded in Fig. 3. The whole process can be divided into 4 stages marked by the ignition of the directly heated 2# LIB. In Stage I between 0~1601 s, the first jet flame emerged from the 2# LIB following the attack of the incident radiative heat flux which ignited the decomposition gases or electrolyte vapor. During Stage II between 1601 s~2760 s, TR was triggered in the 2# LIB at around 2210 s, resulting in a stronger jet flame as shown in Fig. 3c. Figure 5a shows that the HRR reached 22.3 kW at this point; and a sudden loss of 7% of the total mass from the combustible gases were recorded due to the TR. It can also be seen that the jet flame was partially constrained by the solid lower section of the wire mesh shown in Fig. 1. It ignited the 4# LIB, but the flame of the 4# LIB was not sufficiently strong to cause noticeable changes in the measured HRR. When the flame of the 4# LIB extinguished, the 3# LIB self-ignited at 2655 s as shown in Fig. 3d. This was followed by the thermal runaway of the 3# LIB. As shown in Fig. 3e, two jets of white and black smoke can be seen at each side

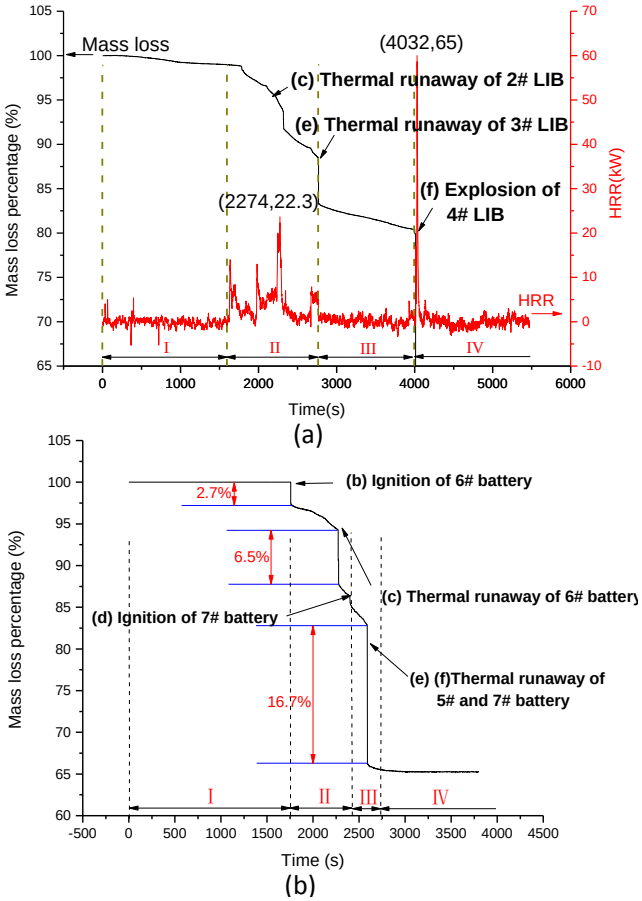

235

Fig. 5 Mass loss and heat release rate curves in two heating tests. (a) the rhombus layout; (b) the parallel layout.

236

237

Following the stable combustion which lasted around 120 s. A loss of nearly 5.2% of the total mass or 20.86% of the 3# LIB mass were recorded in Stage II, which mainly composed of the gases generated during the decomposition of the battery materials and additional electrolyte vapor burned during the processes. Stage III, which was between 2760 s~4011 s, can be regarded as a "smoldering period" with no visible flames or smoke ejection. During this period, the decomposition of the cathode materials in all LIBs continued, especially in the 4# and 1# LIBs, continuously generating combustible gases (mainly hydrocarbons) in the test section which mixed with the ambient air to form a premixed flammable mixture. While the temperatures were initially not sufficiently high to cause ignition, they were continuously increased by the released heat of the 4# and 1# LIBs. This created a hazardous environment with flammable gases premixed with air being raised to above its auto-ignition temperature. At the beginning of Stage IV from 4011 s~end, the 4# LIB exploded, destroying the experimental setup as shown in Figs. 3f and g. The HRR peaked at 65 kW at this moment and the mass loss measurement failed due to the explosion. About 2 minutes later, the 1# LIB also exploded.

The sequence of events in the heating test of the three LIBs in parallel layout can also be divided into four stages marked by the ignition of the 6# LIB as shown in Fig. 4b during stage I from 0~1740 s. In stage II between 1740 s~2400 s, the 6# LIB entered TR following around 540 s of stable combustion as shown in Fig. 4c. This caused 19.38% mass loss from the 6# LIB and 6.5% of mass loss from all the three LIBs. Stage III between 2400 s~2730 s was marked by the ignition of 7# LIB as shown in Fig. 4d. This triggered TR in the 5# LIB at 2690 s as shown in Fig. 4e, but the flame was blew off by the strong smoke flow. While the flow was limited by the lower solid section of the wire mesh and ignited by the flame from the 7# LIB. This limited jet fire of the 5# LIB heated the positive electrode of the 7# LIB and caused a violent ejection of black smoke with vast spark at around 2721

s as shown in Fig. 4f. The TR in Stage III caused 16.7% mass low from all the three LIBs. In stage IV from 2730 s, the flame and smoking extinguished slowly.

3.1.2 The recorded temperature variations and distributions

The measured temperature variations *vs* time during the two heating tests are shown in Figs. 6 and 7.

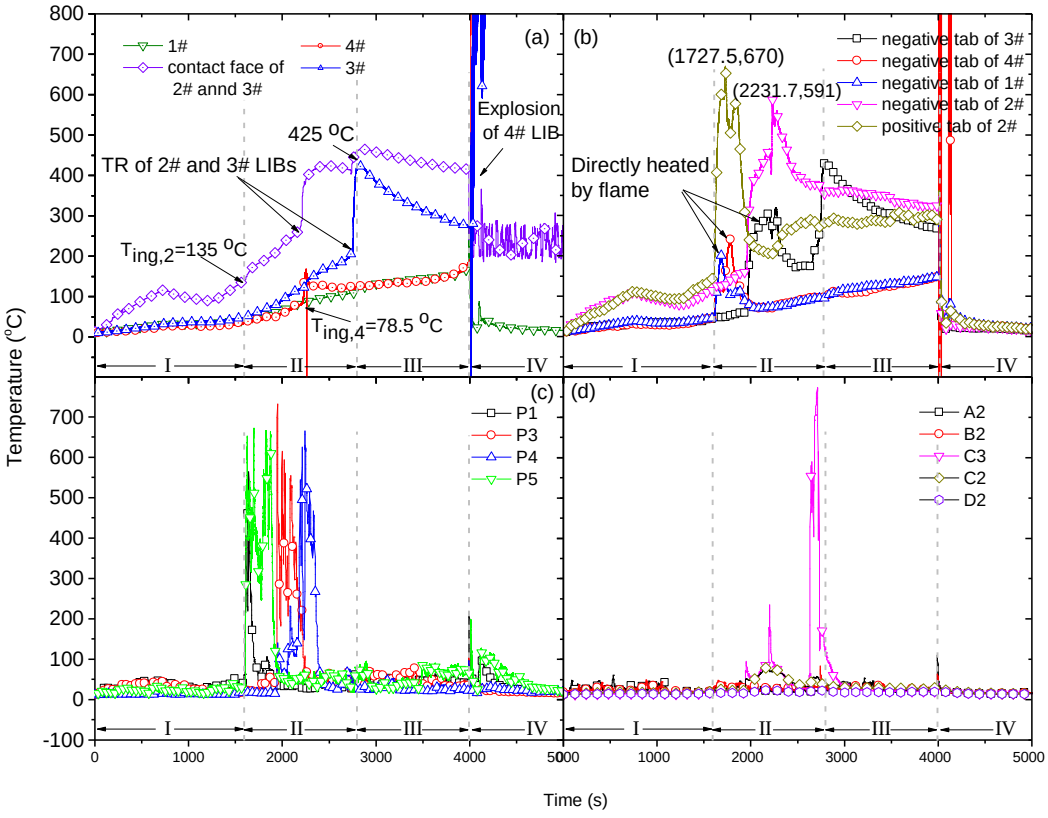

Fig. 6 Temperature history during the heating tests of the four LIBs in rhombus layout: (a) Surface temperature; (b) Tabs' temperature; (c) Ambient temperature in immediate surrounding region; and (d) Ambient temperature in the surrounding region.

As shown in Fig. 6 for the heating test of the LIBs in rhombus layout, the surface temperatures of the 1# and 4# LIBs were close to the ambient temperature in Stage I due to the shading of the boards. In Fig. 6b, the fire from the 2# LIB led to the increase of the tab temperatures of the 1# and 4# batteries to 201 °C and 243 °C, respectively before descending gradually due to heat dissipation. During the TR of the 2# LIB, the violent jet flame ignited the 4# LIB with the surface temperature increased from 78.5 °C to 168 °C at 2254s and caused the temperature at the interface between the 2#

and 3# LIBs in Fig. 6a to increase rapidly from 260 °C to 420 °C. Although the 3# LIB was subjected to heating through the interface with the 2# LIB and radiant heating from the flame, the 4# LIB was ignited ahead of it. A possible explanation was that thermal runaway of the 2# LIB induced a hot spot beside the relief valve of the 4# LIB; and resulted in a local pressure increase and triggered the relief valve. The flame induced fluctuations of the temperature in the immediate and surrounding areas are shown in Figs. 6c and d. At 8 cm from the burning LIB, the temperature reached between 247 °C and 672 °C. The explosion of the 4# LIB caused a sharp increase of the temperature as shown in Figs. 6a and b, damaging all the thermocouples on the surface. Before then, the surface temperature of the 4# LIB increased from 120 °C to 192 °C in Stage III. The transient temperature distribution of the 1# LIB, which was placed symmetrically with the 4# LIB in relation to the 2# LIB, shows a very similar pattern.

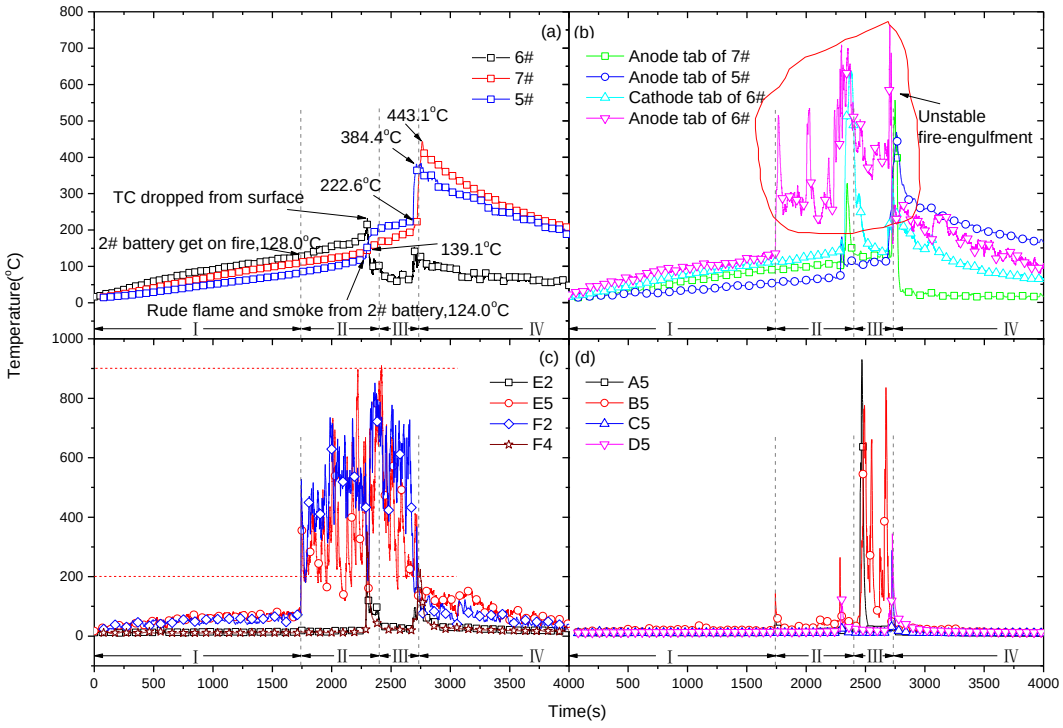

Fig. 7 Temperature history during the heating tests of the four LIBs in parallel layout: (a) Surface temperature; (b) Tabs' temperature; (c) Ambient temperature in immediate surrounding region; and (d) Ambient temperature in the surrounding region.

It was noted that the maximum temperatures recorded in Figs. 6c and 6d are lower than that in

typical hydrocarbon fires. This was because the thermocouple locations were not exactly within the flame envelope. None of the thermocouples used in this study could record the temperature at the time of explosion as their response time was not sufficiently fast.

The temperature history during the heating test of the LIBs in parallel layout is shown in Fig. 7a. It can be seen that during Stage I, the temperature rise of the 7# LIB was faster than that of the 5# LIB (3.3 ℃ min^{-1} vs 2.3 ℃ min^{-1}). This was thought to be because the thinner gypsum board actually has better thermal insulation than the fire-proofing board. In stage II, it was found that the surface temperature of the 5# LIB exceeded that of the 7# LIB; and the temperatures on the cathode and anode tabs of the 6# LIB increased sharply reaching between 200 ℃ and 900 ℃ as shown in Figs. 7b and 7c. As described in the previous section, the jet fire from the 6# LIB was partially constrained by the small solid section of the wire mesh, the recorded temperature fluctuations in the surrounding regions recorded by thermocouples C5 and D5 are relatively small. As the relatively high temperature caused the fixing tape for the Number 4 thermocouple at the center on the surface of the 6# LIB to detach, the temperature at this point was not recorded. The occurrence of TR in the 5# and 7# LIBs caused the surface temperature to increase rapidly from 222 ℃ to 384 ℃ and 200 ℃ to 443 ℃, respectively; and also induced a large fluctuation of temperature on the positive tab sides as well as in the immediate and surrounding regions as shown in Figs. 7b, 7c and 7d.

3.1.3 Comparison and analysis

During the heating tests of both LIB layouts, jet flames are observed and in the test for the rhombus layout, and two of the LIBs exploded. The current tests as well as previous tests all suggest that the TR in one LIB may or may not trigger TR in another LIB within the same battery pack. In terms of flame propagation, LIBs (including the gases released ruing decomposition) in the experimental setup can be regarded as discrete combustibles. In the following analysis, the time of

311 TR propagation to other LIB is defined as the time elapse from the ignition of the 2# and 6# LIBs. As
312 shown in Table 1, the surface temperature at the time of ignition of the 2#, 5#, 6#, 7# LIBs range
313 from 110 °C to 140 °C. These findings are consistent with that of our previous studies [23] in which
314 the LIBs were heated by continuous thermal aggression. It can be seen that the surface temperatures
315 at the time of ignition and TR propagation time of the 1#, 3# and 4# batteries are quite different. This
316 is thought to be because the heating effect from the impinging fire greatly accelerates the
317 thermochemical reaction inside the other LIBs. This finding contradicts the suggestion that flame
318 heating had negligible effect on TR propagation [50]. With flame impingement, the total heat transfer
319 from the flame to the LIBs consists of radiative, convective as well as conductive heat transfer.
320 While in the previous case [23], there was only radiative heat transfer the magnitude of which is also
321 dependent on the geometrical arrangement. In practice, fire-impingement could be a potential
322 hazards for LIB applications in electric vehicles and energy storage in power stations. The
323 temperatures of the tabs were found to be always around 12 ^{o}C lower than the surface temperature
324 whether the particular LIB was on fire or not. In the case of the rhombus layout, the difference
325 between the surface temperatures of the 1# and 4# LIBs was 43^{o}C when the 4# LIB exploded during
326 Stage III in the test. The maximum surface temperature was found to be quite lower than that of the
327 $LiFePO_4$/graphite and NCM/graphite batteries previously tested by the authors' group [51] and others
328 [50]. Except at the time of explosion, the HRR peaks were also found to be lower than these previous
329 tests involving different cathode materials.
330

Table 1 Comparison of parameters associated with thermal and combustion characteristics

No.	$T_{ign,sur}$/ $T_{exp,sur}$ (°C)	$T_{ign,tab}$/ $T_{ign,exp}$(°C)	Ignite Time(s)	T_{max}(°C)	TR time (s)	HRR Peak (kW)	Mass loss ratio (%)
1	--/--	--/--	--	173	--	--	Exploded
2	135/--	116/--	1593	466	0	14/13/22.3	20.9
3	185/--	178/--	2626	425	1033	7.85	30.79
4	78.5/192	73.7/149	2206	192	613	65	Exploded
5	124.1/--	181.1/--	2299.9	384.4	548.9	--	26.1
6	128	135/--	1740	--	0	--	41.6
7	139.1	147.6/--	2326	443.1	586	--	29
Ref. [23]	146.6	121/--	1465	494	--	38	28.9

[a]. As no ignition occurred for the 1# LIB, its $T_{ign,sur}$ and $T_{ign,tab}$ were not detected.

[b]. As the explosion of the 4# LIB destroyed all thermocouples in the surface region, the $T_{exp,\ sur}$ and $T_{exp,tab}$ of the 1# LIB were not detected.

[c]. The T_{ign_tab} only indicate the ignition temperature at the negative tab.

Combining the video recordings of the explosion as shown in Fig. 3f, two possible explanations are postulated as the cause of the explosions of both the 1# and 4# LIBs at such relative low temperatures. One possibility is that these were thermal explosions due to catalytic reactions induced by the elevated temperature inside the LIB. This will be discussed further in the next section. On the other hand, the explosions might also be attributed to BLEVE [52]. As it can be seen from Fig. 3, the 1# and 4# LIBs were engulfed in the flame during Stage II in the test, which heated the electrolyte (liquid). The boiling points of the solvent DMC and DEC are 90.8 ℃ and 118.13 ℃, respectively, both are below the LIB cell surface temperature during Stage III, i.e. the temperature of the electrolyte was well above its boiling point at atmospheric pressure. The boiling of the electrolyte would produce gases which take up far more space than the liquid, resulting in a pressurized liquid and gas mixture (PLG). At some point during Stage III, if the relief valve was suddenly activated due to the elevated temperature above this 'superheat limit temperature'(SLT), there would be instantaneous and homogeneous nucleation, resulting in violent flashing of the electrolyte generating relatively large volume of flammable vapor as shown in Fig. 3g.

A major difference between the present test and some previous tests in which the LIBs did not

explode could possibly be attributed to the difference format of heat impact on the LIBs [17]. In the previous tests [23, 51], the LIBs were heated by a continuous heat flux, which induced the decomposition of the electrolyte and the whole battery system went through thermochemical reaction at elevated temperature. While in the present test, the LIBs were impinged by flame in Stage II, which would have resulted in the decomposition of some but not all of the electrolyte. The decomposition continuously released extra heat to the remaining liquid electrolyte raising its temperature to above its atmospheric-pressure boiling temperature, and resulted in BLEVE in Stage IV.

3.2 Thermal and modeling analysis of the thermal runaway propagation

The thermal analysis of TR propagation below is based on the point that thermochemical reactions at elevated temperature is the main factors that induce the thermal behaviors of lithium ion battery.

3.2.1 Thermochemical reaction and gas production tests

The thermal behavior of LIB depends on the thermochemical characteristics of the materials inside. In order to understand the possibility of LIB explosions due to catalytic reactions induced by the elevated temperature inside the LIB and following on from our previous work [53], the heat flow and gas production of four main reactions [42] were tested separately by the C80 calorimeter mixed in the same proportion as commercial battery as shown in Fig. 8.

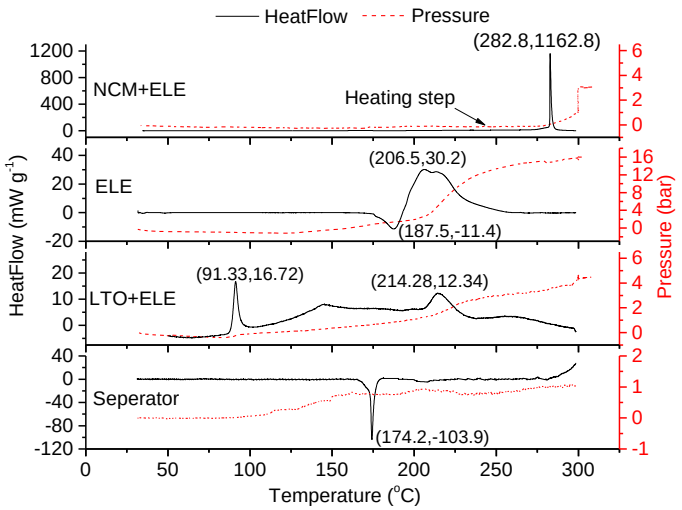

Fig. 8 Heat flow and pressure curves of the electrolyte, separator, cathode (NCM) and anode (LTO) in contact with electrolyte. The mass distribution for pressure tests: 62+33.8 mg for NCM+ELE; 100.8 mg for ELE; 67.9+33.6 mg for LTO+ELE; 6.9 mg for separator.

From the heat flow of NCM material in contact with electrolyte, it was found that a slow rise of the heat flow began from 150 °C and increased sharply from about 250 °C and reached the peak at 282.8 °C. The maximum heat flow was 1162.8 mW g^{-1}. At temperature above 270 °C, following the generation of gases from the thermochemical reactions, the pressure increased rapidly from zero to 3 bar and ended at 5.74 bar in the cooling period. The rapid pressure variation was measured as 0.15 bar per second in the vessel. The volume of the vessel is 3.5 cm^3. According to the ideal gas law, the generation of the gases can be obtained:

$$\frac{P_1 V_1}{T_1} - \frac{P_2 V_2}{T_2} = \Delta n R \quad (1)$$

where P_1, V_1, T_1 are the pressure, volume and temperature of the vessel before heating. P_2, V_2, T_2 are the pressure, volume and temperature of vessel after heating. Δn is the difference in the amount of the gases in the vessel before and after heating. R is the universal gas constant.

The above calculation indicated that the gas generation rate was around 1.24×10^{-4} mol s^{-1} g^{-1}, which was equivalent to 2.77×10^{-3} L s^{-1} g^{-1} at atmosphere pressure. This means if the cathode material and electrolyte together amounts to 15% of the total mass of the battery (1800 g), the gas

generation in this temperature can reach 0.748 L s^{-1}. The rapid generation of the gases and heat has high potential to induce the explosion of the LIB. Roder et al. [54] found a phase transition of the layered material NCM towards a crystalline structure with a space group *Fm*3*m* under this temperature and proposed the overall decomposition reaction:

$$\mathrm{NCM}(R3-m) \xrightarrow{\Delta T, solv.} (\mathrm{Mn,Ni})\mathrm{O}(Fm3m) + \mathrm{CoO} + \mathrm{Ni} + \mathrm{O_2}. \quad (1)$$

The decomposition of the electrolyte has an endothermic process at 187.5 °C, and then turned to exothermic process. The pressure varied along with the two processes and reached 16.2 bar. The endothermic process is mainly considered as the open loop effect of the Lewis acid to EC and the elimination reaction of Lewis acid to solvent [21]. The exothermic process is attributed to the decomposition reaction of the carbonate ester. The endothermic process in the heat flow of the separator indicates the melting of the separator. The maximum pressure in this test reached 1 bar. The heat flow of lithium titanate in contact with the electrolyte shows a small peak at 94.7 °C, which is caused by the decomposition of the solid electrolyte interface (SEI) on the surface of lithium titanate. The maximum pressure reached 4.64 bar. It is interesting to note that the gas production is directly proportional to the quantity of the electrolyte. This is understandable as most of the gas components come from the reduction process and nucleophilic attacks of the electrolyte at elevated temperature [55]. The thermal characteristics of the whole battery materials shown in Fig. 9 can be explained by the above separated tests.

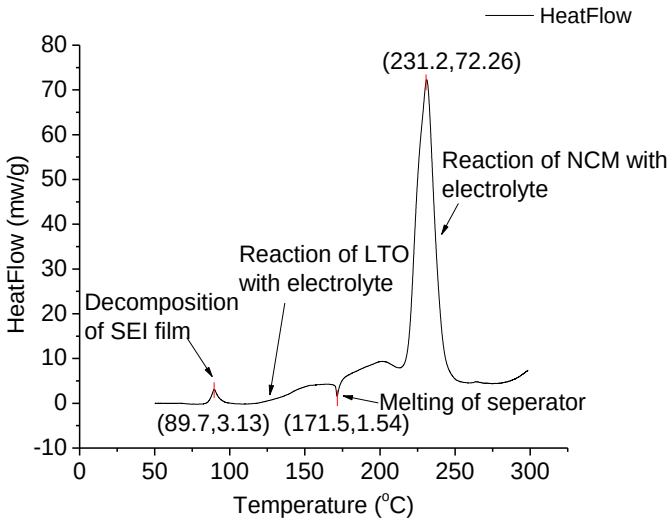

Fig. 9 Heat flow curve of whole battery materials (Reproduced from [53])

As shown in Fig. 8, thermal runaway and explosion of battery can possibly be explained by the violent decomposition of the NCM, represented by the heat flow, when it comes into contact with the electrolyte at 231 °C. The peak temperature in Fig. 9 is ahead of the peak shown in Fig. 8, this could be because the reaction intermediate of the LTO with the electrolyte accelerated the decomposition of the NCM.

Assuming that the Arrhenius law can be applied to these thermochemical reactions, the rate of mass loss of the reactant can be defined for Eq. (1) following our previous analysis [56]:

$$-\frac{\mathrm{d}M}{\mathrm{d}t} = Aexp(-\frac{E}{RT})M^n \tag{2}$$

where *A* is the pre-exponential factor, *E* is the activation energy of reaction, *M* is the mass of reactant and *T* is the temperature of reactant.

At the initial stage, the consumption of the reactant can be ignored. The mass of the reactant could be assumed to equal to the initial mass M_0 in Eq. (2). Multiplying the heat of reaction ΔH, Eq. (2) can be transferred to the heat generation of the reaction:

$$q_G = \frac{\mathrm{d}H}{\mathrm{d}t} = \Delta H M_0^n Aexp\left(-\frac{E}{RT}\right) \tag{3}$$

where q_G is the heat generation rate of reaction and ΔH is the reaction heat. Following Kim et al. [43] and Hatchard et al. [44, 57], the reaction order (n) in the battery system is assumed to be 1.

417 Substituting n = 1 into Eqs. (3), the following can be obtained:

$$\frac{\frac{\mathrm{d}H}{\mathrm{d}t}}{\Delta H M_0} = A exp\left(-\frac{E}{RT}\right) \tag{4}$$

418 Equation (4) can be transformed to (5) by taking logarithm:

$$\ln\left(\frac{\frac{\mathrm{d}H}{\mathrm{d}t}}{\Delta H M_0}\right) = -\frac{E}{R}\frac{1}{T} + \ln A \tag{5}$$

419 Plotting $\ln\left(\frac{\frac{\mathrm{d}H}{\mathrm{d}t}}{\Delta H M_0}\right)$ versus 1/T, the slope and interception point of the curve can be used to

420 calculate the apparent activation energy (E_a) and pre-exponential factor (A). This is shown in Fig. 10

421 using the measurements in the present tests. The calculated reaction kinetic parameters of the three

422 tests in Fig. 10 are listed in Table 2.

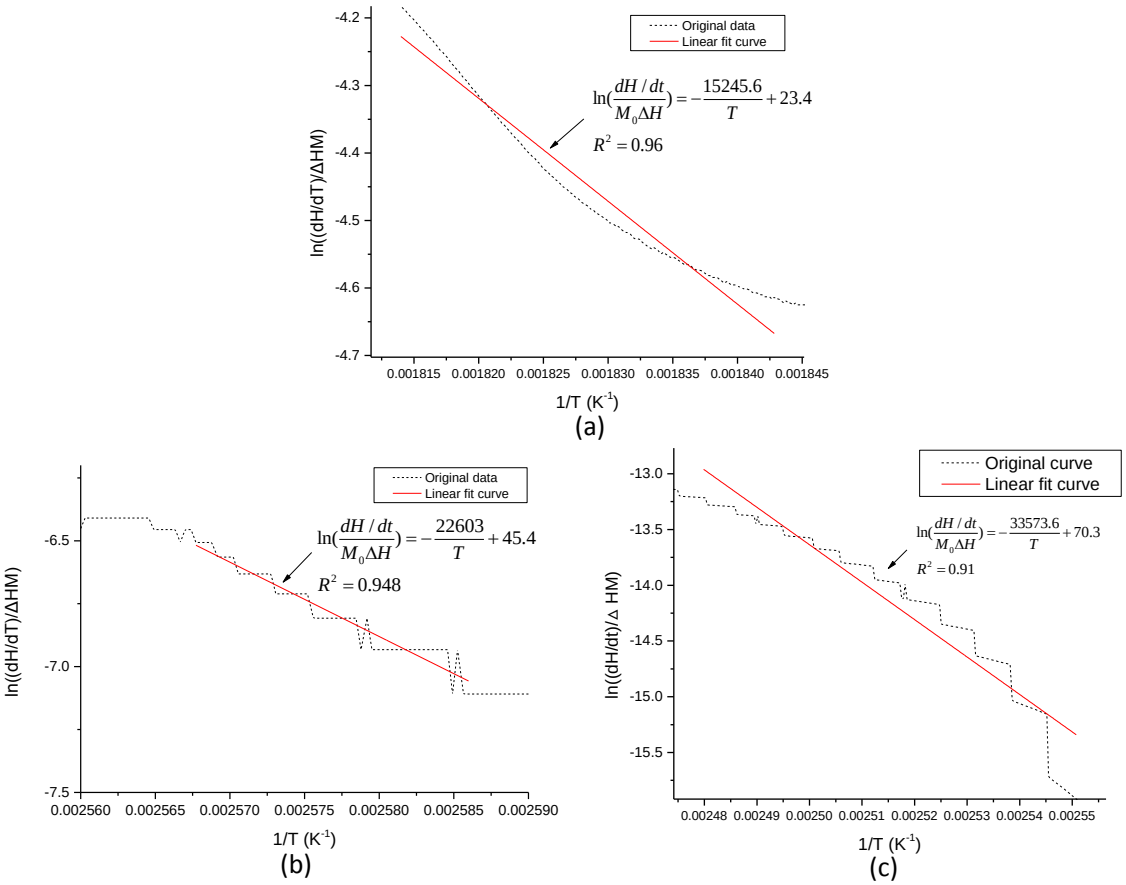

423

424 Fig. 10 The variation of $\ln(\frac{dH/dt}{\Delta H M_0})$ with 1/T. (a) NCM+ELE; (b) LTO+ELE; (c) Total materials

425

Table 2 Chemical reaction kinetic parameters of thermochemical reactions

Materials	Onset temperature (°C)	Peak Temperature (°C)	Peaks (mW g^{-1})	Total heat generation ΔH (J g^{-1})	Apparent activation energy E (kJ mol^{-1})	Pre-exponential factor (A)	R^2
NCM+ELE	218.54	282.76	1162.8	-538.34	126.75	1.5×10^{10}	0.96
LTO+ELE	103	214.3	12.3	-256.87	188	5.21×10^{19}	0.948
Total	116	231.2	72.26	-554.920	279	3.4×10^{30}	0.911

3.2.2 Modeling analysis of thermal runaway propagation

Flame spread between discrete combustibles in a battery module is quite different from typical fire scenarios. As demonstrated experimentally in Section 3.1, the flame of the ignited LIB can affect the surrounding LIBs by heat conduction, radiation or flame impingement. It is difficult to quantify how much energy from the burning LIB can trigger TR in the neighboring cells. However, the critical temperature of the LIB that can accelerate the thermochemical reaction within the inner LIB and result in thermal runaway can be calculated using the Semenov and Frank-Kamenetskii models as shown in Fig. 11 [48, 58]. There are some silent differences between the two models. The Semenov model [65] assumes that the distribution of temperature is uniform in the system and the thermal exchange between system and ambient environment mainly happen on the surface. The Frank-Kamenetskii model [52] assumes that the distribution of the temperature in the system varies with space and time while the gradient of the temperature at the boundary is very small.

The critical temperature is also defined as the self-accelerating decomposition temperature (SADT).

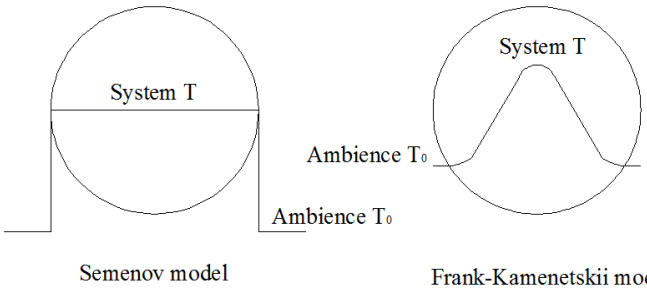

Fig. 11 The temperature distribution in Semenov and Frank-Kamenetskii models (Reproduced from [59])

The boundary condition could be expressed as:

$$\frac{\lambda \mathrm{d}T}{\mathrm{d}r} + \chi(T_\mathrm{s} - T_\mathrm{a}) = 0, r = a_0 \tag{6}$$

where λ is the heat transfer coefficient, χ is the equivalent surface heat transfer coefficient, T_s is the surface temperature of cell and T_a is the ambient temperature.

The above equation can be non-dimensionalized as:

$$\frac{\mathrm{d}\theta}{\mathrm{d}\rho} + Bi\theta = 0, \rho = 1 \tag{7}$$

where *Bi* is the ratio of the internal thermal resistance to the thermal resistance at boundary layer and it equals to $\chi\alpha_0/\lambda$. In the Semenov model[47, 59], the *Bi* was close to zero. Thus, the boundary condition can be obtained from Eq. (7):

$$\frac{\mathrm{d}\theta}{\mathrm{d}\rho} = 0, \rho = 1 \tag{8}$$

From the center to the boundary $(0 < \rho < 1)$, $\frac{\mathrm{d}\theta}{\mathrm{d}\rho}$ equals to zero.

Equation (7) can be re-written as:

$$\frac{1}{Bi}\frac{\mathrm{d}\theta}{\mathrm{d}\rho} + \theta = 0 \tag{9}$$

In the Frank-Kamenetskii model [52], the *Bi* parameter approaches infinity. So, the boundary condition is $\theta = 0$. At the center ($\rho = 0$), the temperature gradient ($\frac{\mathrm{d}\theta}{\mathrm{d}\rho}$) equals to zero.

Assuming that the components of cells are in homogeneous distribution, the cathode, anode materials, separator and electrolyte compose of a minimum unit in large format LIB as shown in Fig. 12[60]. Exponential approximation (reaction function $\mathrm{f}(\theta)$ equals to e^{θ}) is applied to the reactions

457 in both models.

458 Table 3 The thickness and physical properties of the battery materials

Materials	NCM	Separator	LTO	Al Foil
Thickness, mm	0.1	0.025	0.1	0.024
Density, kg m^{-3}	1500	1200	3510	2702
Thermal conductivity, W m^{-1} K^{-1}	5	1	1.04	238

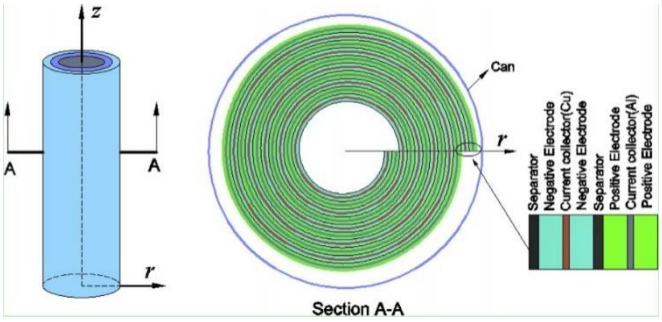

459 Fig. 12 Schematic of the cross-section of a cylindrical lithium-ion single battery (Reproduced from [60]).

460 Table 3 lists the thicknesses and physical properties of the battery materials. The overall heat transfer
461 coefficient λ_{ave} was calculated through Matlab software following the formulations for composite
462 cylinders as 1.64 W m^{-1} K^{-1}:

$$\frac{\ln\left(\frac{r_b}{r_1}\right)}{\lambda_{ave}} = \frac{\ln\left(\frac{r_1+d_s}{r_1}\right)}{\lambda_s} + \frac{\ln\left(\frac{r_1+d_s+d_n}{r_1+d_s}\right)}{\lambda_n} + \frac{\ln\left(\frac{r_1+d_s+d_n+d_c}{r_1+d_s+d_n}\right)}{\lambda_c}$$
$$+ \frac{\ln(\frac{d_1+d_s+d_n+d_c+d_n}{r_1+d_s+d_n+d_c})}{\lambda_n} + \frac{\ln(\frac{r_1+d_s+d_n+d_c+d_n+d_s}{r_1+d_s+d_n+d_c+d_n})}{\lambda_s} + \frac{\ln(\frac{r_1+d_s+d_n+d_c+d_n+d_s+d_p}{r_1+d_s+d_n+d_c+d_n+d_s})}{\lambda_p}$$
$$+ \frac{\ln(\frac{r_1+d_s+d_n+d_c+d_n+d_s+d_p+d_c}{r_1+d_s+d_n+d_c+d_n+d_s+d_p})}{\lambda_c} + \frac{\ln(\frac{r_1+d_s+d_n+d_c+d_n+d_s+d_p+d_c+d_p}{r_1+d_s+d_n+d_c+d_n+d_s+d_p+d_c})}{\lambda_p}$$
$$+ \frac{\ln(\frac{r_1+d_u+d_s}{r_1+d_u})}{\lambda_s} + \frac{\ln(\frac{r_1+d_u+d_s+d_n}{r_1+d_u+d_s})}{\lambda_n} + \overbrace{\cdots\cdots}^{i} + \frac{\ln(\frac{r_1+i*d_u+d_s+d_n+d_c+d_n+d_s+d_p+d_c}{r_1+i*d_u+d_s+d_n+d_c+d_n+d_s+d_p})}{\lambda_c}$$
$$+ \frac{\ln(\frac{r_1+i*d_u+d_s+d_n+d_c+d_n+d_s+d_p+d_c+d_p}{r_1+i*d_u+d_s+d_n+d_c+d_n+d_s+d_p+d_c})}{\lambda_p} \quad (10)$$

463 where r_b is the radius of cell, r_1 is the radius of mandrel that equals to 4mm, d_s, d_n, d_p, d_c are the
464 thickness of separator, anode material, cathode material and collector, respectively, d_u is the total
465 thickness of a minimum unit that equals to $2\times(d_s+d_n+d_p+d_c)$. λ_{ave} is the average thermal

conductivity of total materials inside the cell; λ_s, λ_n, λ_p, λ_c are thermal conductivity of separator, anode material, cathode material and collector, respectively. *i* is the layers of a minimum unit, equals to 56. Because the electrolyte infiltrated into electrode materials and separator, above calculation don't contain the heat transfer of electrolyte.

The thermal resistant on boundary layer is composed of natural convection and radiation. A parameter χ is defined as:

$$\chi = h + \varepsilon\sigma(T_s^2 + T_a^2)(T_s + T_a) \quad (11)$$

where the natural convective heat transfer coefficient of air (h) is between 5 to 25 W/(m^2 K). The emissivity of cells (ε) should equal to the can (ε =0.3); σ is the Stefan-Boltzmann constant ($\sigma = 5.67 \times 10^{-8}$ W m^{-2}K^{-4}.

When T_s is 373K, the second term on the right hand side term in Eq.(10) was calculated as 2.35 W m^{-2}K^{-1}. χ is taken 10 W m^{-2}K^{-1}. The following analysis of natural convection and radiation. The dimensionless *Bi* number of the battery can be obtained as:

$$Bi = \frac{10 \times 0.033}{1.64} = 0.2 \quad (12)$$

When *Bi* parameter is between 0 and 0.2, it is feasible to calculate the critical temperature of the ambient air using the Semenov model [59]. In this case, the battery temperature is uniform in space distribution. As shown in Fig. 13, when the heat dissipation curve (q_L) tangents to the exothermal curve (q_G), the corresponding ambient temperature T_{02} is the SADT of the battery. The temperature of the tangent point E is named as the temperature of no-return (T_{NR}).

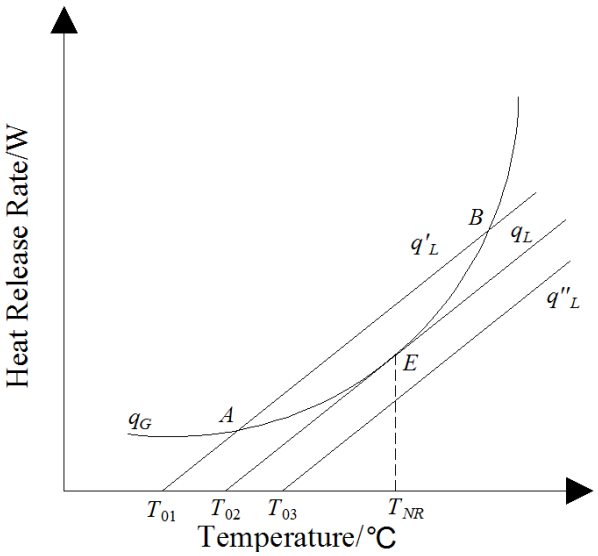

Fig. 13 Illustration of thermal equilibrium in the Semenov model [59].

At the tangent point E, the heat generation is balanced by the dissipation:

$$\Delta HMAexp\left(-\frac{E_a}{RT_{NR}}\right) = \chi S(T_{NR} - T_0) \quad (13)$$

Take differentiations of both sides of Eq. (13):

$$\Delta HMAexp\left(-\frac{E_a}{RT_{NR}}\right)\left(\frac{E_a}{RT_{NR}^2}\right) = \chi S \quad (14)$$

To calculate T_{NR}, Eq. (14) can be solved by iterative method by re-writing it as:

$$T_{NR(n+1)} = \frac{E_a}{Rln(\frac{\Delta HMAE_a}{\chi SRT_{NR(n)}^2})} \quad (15)$$

where $T_{NR(n)}$ and $T_{NR(n+1)}$ are the temperatures of no return at step n and n+1 during the iteration process.

Substituting the above parameters into Eq. (15) and iterating for the temperature with the Matlab software, T_{NR} = 131 ^{o}C is obtained. Dividing Eq. (13) by Eq. (14), the following is obtained:

$$\frac{RT_{NR}^2}{E_a} = T_{NR} - T_0 \quad (16)$$

Thus $T_{0,}$ which is also the self-accelerate decomposition temperature under Semenov model ($SADT_{sem}$), can be obtained by:

$$\mathrm{SADT_{sem}} = T_{\mathrm{NR}} - \frac{RT_{\mathrm{NR}}^2}{E_{\mathrm{a}}} = 126.1\ ℃ \tag{17}$$

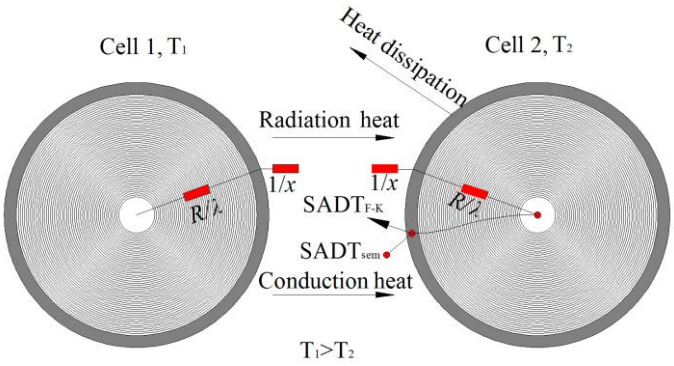

Fig. 14 Illustration of thermal runaway in a representative two cylindrical cell system. Cell 1 is under thermal runaway.

This result indicates that the battery would self-ignite when the ambient temperature exceeds 126.1 °C. When the LIB is subjected to external heating or engulfed in a fire; the heat dissipation and thermal resistance at the boundary layer would sharply decrease, this could accelerate the internal reactions and reduce the delay time of thermal runaway. In this case, it could be more effective to regard the shell of the LIB as the boundary condition for the materials inside to calculate the critical temperature through the Frank-Kamenetskii model [52]. The SADT of the LIB indicates the lowest temperature of the shell that could induce thermal runaway of the inner materials. If the shell temperature is above the critical temperature and the time is also beyond the delay time of TR that from when cells satisfy the critical condition to thermal runaway, TR would propagate in the battery module as shown in Fig. 14.

Frank-Kamenetskii model [52] and considering the internal heat transfer inside the LIB, the heat balance equation can be written as:

$$\rho C_{\mathrm{p}} \frac{\partial T}{\partial t} = \lambda_{\mathrm{ave}} \Delta T^2 + \Delta H \rho^n A exp\left(-\frac{E}{RT}\right) \tag{18}$$

where ρ is the average density of the battery materials. C_{p} is the specific heat of the LIB. The Frank-Kamenetskii critical parameter δ_{cr} is defined following Kamenetskii [58] to take the

non-dimensionalised form of Eq. (18):

$$\delta_{\mathrm{cr}} = \frac{a_0^2 \Delta H E \rho^n A exp\left(-\frac{E}{RT_0}\right)}{\lambda R T_0^2} \tag{19}$$

where T_0 is the shell temperature which is equal to the self-accelerate decomposition temperature under Frank-Kamenetskii model ($SADT_{F\text{-}K}$). a_0 is the reactantive characteristic dimension of the object.

The LIB sample is a cylinder of length (l) × diameter (d), and in this particular case 260 mm × 66 mm.

In such finite cylinder (l>d), the Frank-Kamenetskii critical parameter can be calculated by the following equation as $\delta_{\mathrm{cr}} = 2.05$ by:

$$\delta_{\mathrm{cr}} = 2.0 + 0.78(d/l)^2 \tag{20}$$

To calculate the $SADT_{F\text{-}K}$, Eq. (19) can be re-written as:

$$T_{0(i+1)} = \frac{E}{R \ln\left(\frac{a_0^2 \Delta H E c_0^n A}{\delta_{\mathrm{cr}} \lambda_{\mathrm{ave}} R T_{0(i)}^2}\right)} \tag{21}$$

where $T_{0(n)}$ and $T_{0(n+1)}$ are the shell temperature at step n and n+1 during the iteration calculation. The average density of the battery materials is $\rho = 1832$ kg m^{-3}.

Substituting the above parameters into Eq. (21) and iterating for the temperature, the $SADT_{F\text{-}K}$ of the NCM-LTO battery was found to be $SADT_{F\text{-}K}$ = 139.2 °C. It should be mentioned that, the SADT calculated by the Frank-Kamenetskii model is mainly appropriate for the situation that the Bi approaches infinity such as fire-engulfment. For other situations, the value should be higher. We can also calculate the SADT of the cell in two stages at different temperature regions by dividing the total reaction into two thermochemical reactions on the anode and cathode materials. This way, the total heat generation of the two electrode reactions should multiply 0.4 in a whole cell as only 40

528 percentage of the space in the cell generates heat according to the relative thickness of electrode
529 materials. The SADTs of LTO and NCM electrodes in contact with electrolyte calculated by the
530 Semenov model [65] are found to be 123.1 and 160.1 °C, respectively. While the corresponding
531 values calculated by the Frank-Kamenetskii model are 142.6 and 196.6 °C. These results show that if
532 the energy from the burnt battery is sufficient to make the ambient temperature over 126.1 °C or heat
533 the surrounding batteries to 139.2 °C, and the time beyond the delay time of TR, TR would propagate
534 from the failure cell to the surrounding cells although the thermal runaway progress of failure cell
535 finished. Furthermore, if the module does not cool down before the shell temperature reaches
536 196.6 °C or the surrounding temperature reaches 160.1 °C, it would be hard to halt the rapid
537 generation of heat and gas due to the self-accelerating decomposition of NCM in contact with the
538 electrolyte. From the results of their oven exposure tests and computational analysis, Lopez [17] and
539 Hatchard et al. [44] commented that when the ambient temperature is beyond the SADT the battery
540 system is in supercritical situation and the delay time to thermal runaway would decrease with the
541 increase of ambient temperature. On the contrary, below the critical condition, it would be hard for
542 TR to propagate between the battery cells and the TR delay time would approach infinity.

543 During the heating test for the rhombus layout, the 4# battery exploded after nearly 20 minutes
544 of flameless situation in stage Ⅲ. This could be attributed to the self-accelerating reactions inside
545 the battery which are similar to smoldering combustion. These reactions continue to produce heat
546 which further increased the temperature of the system. Figure 6 shows that the surface temperature
547 of the 1# and 4# cells were between 120 °C and 130 °C after all the flames extinguished. These are
548 close to the above SADTs predicted by the Semenov [47] and Frank-Kamenetskii models [48]. It
549 should be bearing in mind that there are some underlying model assumptions which would affect the
550 accuracy of the predictions. Both models were developed for a single reaction system. When it is

551 applied here, the multiple reactions in the LIB is treated as an overall reaction and homogeneous
552 distribution of the cell materials is assumed. In addition, the calculation was based on the C80
553 experiments data with a heating rate of 0.2^{o}C/min. It is known that the heating speed affects the onset
554 temperature of the reactant, which would in turn influence the calculation of the pre-exponent factor
555 and activation energy. More experiments with different heating rates and thermal abuse tests as ARC
556 and hot box will be useful to improve the calculation and even refining the models.

557 **4. Conclusions**

558 The thermal and combustion characteristics of flame propagation over the battery module were
559 investigated through heating tests of large format LIBs arranged in rhombus and parallel layouts.
560 Such batteries have already been used commercially for energy storage while relatively little is
561 known about its safety features in connection with potential runaway caused fire and explosion
562 hazards. It was found in the present heating tests that flame heating had considerable effects on TR
563 propagation. Different from previous tests in which the LIBs were subject to continuous constant
564 heating, the impingement of the fire aggravated the combustion behavior and even induced explosion
565 after a "smoldering period" in stage III of test for the rhombus layout. The relatively large
566 fluctuations of temperature in the immediate surroundings between 200 ^{o}C and 900 ^{o}C greatly
567 accelerated the thermochemical reaction inside the LIB, resulting in rapid temperature rise
568 electro-chemical reactions inside the cathode and anode materials. The events leading to the
569 explosions in the test for the rhombus layout was further analyzed and two possible explanations
570 were postulated and analyzed based on either internal catalytic reactions or BLEVE. The later was
571 thought to be a possibility as the measured LIB cell surface temperatures were higher than the
572 boiling points of the electrolyte liquid. The resulting boiling of the electrolyte would produce gases
573 and increasing of the internal pressure, activating the relief valve and producing violent flashing of

574 the electrolyte.

575 In order to explore further the possible cause of the explosions due to catalytic reactions, thermal
576 and gas generation analysis through separate tests of samples of the anode and cathode materials
577 have revealed that a series of reactions could prevail inside the LIBs tested. The sudden
578 transformation from the stable flame to radical ejection or even explosion during the combustion was
579 likely caused by the reaction between the NCM and electrolyte when the temperature exceeded
580 260 $^{\circ}$C, resulting in rapid generation of heat (1162.8 mW g^{-1}) and gases (2.77×10^{-3} L s^{-1} g^{-1}). In order
581 to estimate the minimum temperature required to induce TR in the LIB and trigger self-ignition, the
582 classical models of Semenov [47] and Frank-Kamenetskii [48] have been applied for the first time to
583 shade further light on the thermal runaway of LIB and TR propagation. The $SADT_{sem}$ and $SADT_{F\text{-}K}$
584 were calculated as 126.1 ^{o}C and 139.2 ^{o}C, indicating that slow self-accelerating reactions, similar to
585 smoldering combustion, occurred inside the 1# and 4# cells in the "smoldering period" before the
586 batteries exploded. This finding suggested that there could be potential of TR propagation over
587 neighboring cells when the critical condition based on SADT was reached. The small discrepancies
588 between the measured cell surface temperatures and the predicted SADT by the two models could be
589 possibly attributed to the underlying assumptions in the two models and the fact that the
590 temperatures measured were on the LIB cell surface while the temperatures inside the LIBs could be
591 higher and closer to the predictions of the two models.

592 The above new insight of TR and TR propagation can aid the design of the pre-warning system
593 in large scale energy storage systems using LIBs. For example, fireproof and heat insulation
594 measures could be used to prevent the temperature of the cell to reach the critical condition.
595 Firefighters should also be cautioned about the potential of TR propagation and even explosions in
596 battery modules after the initial fire appears to be extinguished. Moreover, the results also suggest

that the materials with slower and fewer heat generation should be safer because their higher critical temperature, which can delay the time to TR.

Although the pioneering analysis using the Semenov [47] and Frank-Kamenetskii [48] models were conducted with the NCM/LTO large format battery, the methodology could be applied to analyze other LIBs. Being relatively simple, the computational efficiency was also an advantage over detailed numerical simulations.

Acknowledgements

This work is supported by the National Natural Science Foundation of China (No. 51176183), National Key Research Program (No. 2016YFB0100305), the External Cooperation Program of BIC, CAS (No. 211134KYSB20150004) and the Fundamental Research Funds for the Central Universities (No. WK2320000034). Dr. Q.S Wang is supported by Youth Innovation Promotion Association CAS (No.2013286). Dr P. Ping is supported by the Incoming International Fellowship grant (No. 656582) of the European Commission's Marie Curie Action.

References

[1] Armand M, Tarascon JM. Building better batteries. Nature. 2008;451:652-7.
[2] Scrosati B, Hassoun J, Sun YK. Lithium-ion batteries. A look into the future. Energy & Environmental Science. 2011;4:3287-95.
[3] Bandhauer TM, Garimella S, Fuller TF. A Critical Review of Thermal Issues in Lithium-Ion Batteries. Journal of The Electrochemical Society. 2011;158:R1.
[4] Doughty D, Peter Roth E. A general discussion of Li ion battery safety. The Electrochemical Society Interface. 2012.
[5] Takami N, Inagaki H, Kishi T, Harada Y, Fujita Y, Hoshina K. Electrochemical Kinetics and Safety of 2Volt Class Li-Ion Battery System Using Lithium Titanium Oxide Anode. Journal of the Electrochemical Society. 2009;156:215-351.
[6] Takami N, Inagaki H, Tatebayashi Y, Saruwatari H, Honda K, Egusa S. High-power and long-life lithium-ion batteries using lithium titanium oxide anode for automotive and stationary power applications. Journal of Power Sources. 2013;244:469-75.
[7] Cohen S, Gulbinska MK, Puglia FJ. Lithium-ion Cell and Battery Safety. 2014:115-50.
[8] Lisbona D, Snee T. A review of hazards associated with primary lithium and lithium-ion batteries. Process Safety and Environmental Protection. 2011;89:434-42.
[9] Ouyang M, Ren D, Lu L, Li J, Feng X, Han X, et al. Overcharge-induced capacity fading analysis for large format lithium-ion batteries with Li y Ni 1/3 Co 1/3 Mn 1/3 O 2+ Li y Mn 2 O 4 composite cathode. Journal of Power Sources. 2015;279:626-35.
[10] Ouyang M, Zhang M, Feng X, Lu L, Li J, He X, et al. Internal short circuit detection for battery pack using equivalent

parameter and consistency method. Journal of Power Sources. 2015;294:272-83.
[11] Larsson F, Mellander B-E. Abuse by external heating, overcharge and short circuiting of commercial lithium-ion battery cells. Journal of The Electrochemical Society. 2014;161:A1611-A7.
[12] Lamb J, Orendorff CJ, Amine K, Krumdick G, Zhang Z, Zhang L, et al. Thermal and overcharge abuse analysis of a redox shuttle for overcharge protection of LiFePO 4. Journal of Power Sources. 2014;247:1011-7.
[13] Doh C-H, Kim D-H, Kim H-S, Shin H-M, Jeong Y-D, Moon S-I, et al. Thermal and electrochemical behaviour of C/Li x CoO 2 cell during safety test. Journal of Power Sources. 2008;175:881-5.
[14] Leising RA, Palazzo MJ, Takeuchi ES, Takeuchi KJ. Abuse testing of lithium-ion batteries: Characterization of the overcharge reaction of licoo2/graphite cells. Journal of The Electrochemical Society. 2001;148:A838-A44.
[15] Roth E, Doughty D, Franklin J. DSC investigation of exothermic reactions occurring at elevated temperatures in lithium-ion anodes containing PVDF-based binders. Journal of power sources. 2004;134:222-34.
[16] Lamb J, Orendorff CJ. Evaluation of mechanical abuse techniques in lithium ion batteries. Journal of Power Sources. 2014;247:189-96.
[17] Lopez CF, Jeevarajan JA, Mukherjee PP. Characterization of Lithium-Ion Battery Thermal Abuse Behavior Using Experimental and Computational Analysis. Journal of The Electrochemical Society. 2015;162:A2163-A73.
[18] Leising RA, Palazzo MJ, Takeuchi ES, Takeuchi KJ. Abuse Testing of Lithium-Ion Batteries: Characterization of the Overcharge Reaction of LiCoO[sub 2]/Graphite Cells. Journal of The Electrochemical Society. 2001;148:A838.
[19] Abraham DP, Roth EP, Kostecki R, McCarthy K, MacLaren S, Doughty DH. Diagnostic examination of thermally abused high-power lithium-ion cells. Journal of Power Sources. 2006;161:648-57.
[20] Zhao R, Liu J, Gu J. Simulation and experimental study on lithium ion battery short circuit. Applied Energy. 2016;173:29-39.
[21] Gachot G, Grugeon S, Armand M, Pilard S, Guenot P, Tarascon J-M, et al. Deciphering the multi-step degradation mechanisms of carbonate-based electrolyte in Li batteries. Journal of Power Sources. 2008;178:409-21.
[22] Wang Q, Ping P, Zhao X, Chu G, Sun J, Chen C. Thermal runaway caused fire and explosion of lithium ion battery. Journal of Power Sources. 2012;208:210-24.
[23] Huang P, Wang Q, Li K, Ping P, Sun J. The combustion behavior of large scale lithium titanate battery. Scientific reports. 2015;5:7788.
[24] Cabrera-Castillo E, Niedermeier F, Jossen A. Calculation of the state of safety (SOS) for lithium ion batteries. Journal of Power Sources. 2016;324:509-20.
[25] Beelen H, Raijmakers L, Donkers M, Notten P, Bergveld H. A comparison and accuracy analysis of impedance-based temperature estimation methods for Li-ion batteries. Applied Energy. 2016;175:128-40.
[26] Feng X, Ai X, Yang H. A positive-temperature-coefficient electrode with thermal cut-off mechanism for use in rechargeable lithium batteries. Electrochemistry communications. 2004;6:1021-4.
[27] Balakrishnan P, Ramesh R, Kumar TP. Safety mechanisms in lithium-ion batteries. Journal of Power Sources. 2006;155:401-14.
[28] Zhang G, Cao L, Ge S, Wang CY, Shaffer CE, Rahn CD. Reaction temperature sensing (RTS)-based control for Li-ion battery safety. Scientific reports. 2015;5:18237.
[29] Zhang SS. A review on the separators of liquid electrolyte Li-ion batteries. Journal of Power Sources. 2007;164:351-64.
[30] Feng X, Weng C, Ouyang M, Sun J. Online internal short circuit detection for a large format lithium ion battery. Applied Energy. 2016;161:168-80.
[31] Lopez CF, Jeevarajan JA, Mukherjee PP. Experimental Analysis of Thermal Runaway and Propagation in Lithium-Ion Battery Modules. Journal of the Electrochemical Society. 2015;162:A1905-A15.
[32] Ping P, Wang QS, Huang PF, Sun JH, Chen CH. Thermal behaviour analysis of lithium-ion battery at elevated temperature using deconvolution method. Applied Energy. 2014;129:261-73.
[33] Jhu C-Y, Wang Y-W, Wen C-Y, Shu C-M. Thermal runaway potential of LiCoO2 and Li(Ni1/3Co1/3Mn1/3)O2 batteries

675 determined with adiabatic calorimetry methodology. Applied Energy. 2012;100:127-31.
676 [34] Roth E, Doughty D. Thermal abuse performance of high-power 18650 Li-ion cells. Journal of power sources.
677 2004;128:308-18.
678 [35] Liu X, Stoliarov SI, Denlinger M, Masias A, Snyder K. Comprehensive calorimetry of the thermally-induced failure of
679 a lithium ion battery. Journal of Power Sources. 2015;280:516-25.
680 [36] Finegan DP, Scheel M, Robinson JB, Tjaden B, Hunt I, Mason TJ, et al. In-operando high-speed tomography of
681 lithium-ion batteries during thermal runaway. Nature communications. 2015;6:6924.
682 [37] Feng X, Sun J, Ouyang M, He X, Lu L, Han X, et al. Characterization of large format lithium ion battery exposed to
683 extremely high temperature. Journal of Power Sources. 2014;272:457-67.
684 [38] Spotnitz RM, Weaver J, Yeduvaka G, Doughty DH, Roth EP. Simulation of abuse tolerance of lithium-ion battery
685 packs. Journal of Power Sources. 2007;163:1080-6.
686 [39] Smyshlyaev A, Krstic M, Chaturvedi N, Ahmed J, Kojic A. PDE model for thermal dynamics of a large Li-ion battery
687 pack. American Control Conference (ACC), 2011: IEEE; 2011. p. 959-64.
688 [40] Lamb J, Orendorff CJ, Steele LAM, Spangler SW. Failure propagation in multi-cell lithium ion batteries. Journal of
689 Power Sources. 2015;283:517-23.
690 [41] Ribière P, Grugeon S, Morcrette M, Boyanov S, Laruelle S, Marlair G. Investigation on the fire-induced hazards of
691 Li-ion battery cells by fire calorimetry. Energy & Environmental Science. 2012;5:5271-80.
692 [42] Feng X, Fang M, He X, Ouyang M, Lu L, Wang H, et al. Thermal runaway features of large format prismatic lithium
693 ion battery using extended volume accelerating rate calorimetry. Journal of Power Sources. 2014;255:294-301.
694 [43] Roth EP. Abuse response of 18650 Li-ion cells with different cathodes using EC: EMC/LiPF6 and EC: PC: DMC/LiPF6
695 electrolytes. ECS Transactions. 2008;11:19-41.
696 [44] Hatchard TD, MacNeil DD, Basu A, Dahn JR. Thermal Model of Cylindrical and Prismatic Lithium-Ion Cells. Journal of
697 The Electrochemical Society. 2001;148:A755.
698 [45] Sun JH, Li YF, Hasegawa K. A study of self-accelerating decomposition temperature (SADT) using reaction
699 calorimetry. Journal of Loss Prevention in the Process Industries. 2001;14:331-6.
700 [46] Roduit B, Hartmann M, Folly P, Sarbach A, Brodard P, Baltensperger R. Determination of thermal hazard from DSC
701 measurements. Investigation of self-accelerating decomposition temperature (SADT) of AIBN. Journal of Thermal
702 Analysis and Calorimetry. 2014;117:1017-26.
703 [47] Semenov NN. Some Problems of Chemical Kinetics and Reactivity: Pergamon Press; 1958.
704 [48] Frank-Kamenetskii DA, Semenov NN, Wilhelm RH. Diffusion and Heat Exchange in Chemical Kinetics: Princeton
705 University Press; 1955.
706 [49] Wang QS, Sun JH, Chen CH. Effects of solvents and salt on the thermal stability of lithiated graphite used in lithium
707 ion battery. Journal of hazardous materials. 2009;167:1209-14.
708 [50] Feng XN, Sun J, Ouyang MG, Wang F, He XM, Lu LG, et al. Characterization of penetration induced thermal runaway
709 propagation process within a large format lithium ion battery module. Journal of Power Sources. 2015;275:261-73.
710 [51] Ping P, Wang QS, Huang PF, Li K, Sun JH, Kong DP, et al. Study of the fire behavior of high-energy lithium-ion
711 batteries with full-scale burning test. Journal of Power Sources. 2015;285:80-9.
712 [52] Abbasi T, Abbasi SA. The boiling liquid expanding vapour explosion (BLEVE): Mechanism, consequence assessment,
713 management. Journal of Hazardous Materials. 2007;141:489-519.
714 [53] Wu K, Feng L, Chen M, Li Y, Liu B, Peng P, et al. Thermal Stability Analysis on Li(NixCoyMnz)O2/Li4Ti5O12 Battery.
715 Chinese Journal of Materials Research. 2014.
716 [54] Röder P, Baba N, Wiemhöfer HD. A detailed thermal study of a Li[Ni0.33Co0.33Mn0.33]O2/LiMn2O4-based lithium
717 ion cell by accelerating rate and differential scanning calorimetry. Journal of Power Sources. 2014;248:978-87.
718 [55] Gachot G, Grugeon S, Eshetu GG, Mathiron D, Ribiere P, Armand M, et al. Thermal behaviour of the
719 lithiated-graphite/electrolyte interface through GC/MS analysis. Electrochimica Acta. 2012;83:402-9.
720 [56] Sun J, Sun Z, Wang Q, Hui D, Tong W, Jiang C. Catalytic effects of inorganic acids on the decomposition of

721 ammonium nitrate. Journal of hazardous materials. 2005;127:204-10.
722 [57] Kim G-H, Pesaran A, Spotnitz R. A three-dimensional thermal abuse model for lithium-ion cells. Journal of Power
723 Sources. 2007;170:476-89.
724 [58] Fisher HG, Goetz DD. Determination of Self-Accelerating Decomposition Temperatures for Self-Reactive Substances.
725 Journal of Loss Prevention in the Process Industries. 1993;6:183-94.
726 [59] Feng C. Thermal Theory of Explosion. Beijing: Science Press; 1988.
727 [60] Yang N, Zhang X, Li G, Hua D. Assessment of the forced air-cooling performance for cylindrical lithium-ion battery
728 packs: A comparative analysis between aligned and staggered cell arrangements. Applied Thermal Engineering.
729 2015;80:55-65.
730
731
732